

Embedded Microbubbles for Acoustic Manipulation of Single Cells and Microfluidic Applications

Nino F. Läubli,^{*,†,||} Michael S. Gerlt,^{‡,||} Alexander Wüthrich,[†] Renard T. M.
Lewis,[¶] Naveen Shamsudhin,[†] Ulrike Kutay,[¶] Daniel Ahmed,^{†,§} Jürg Dual,[‡] and
Bradley J. Nelson[†]

[†]*Multi-Scale Robotics Lab, Institute of Robotics and Intelligent Systems, Department of
Mechanical and Process Engineering, ETH Zurich, Zurich, Switzerland*

[‡]*Mechanics and Experimental Dynamics, Institute of Mechanical Systems, Department of
Mechanical and Process Engineering, ETH Zurich, Zurich, Switzerland*

[¶]*Institute of Biochemistry, Department of Biology, ETH Zurich, Zurich, Switzerland*

[§]*Acoustic Robotics for Life Sciences and Healthcare, Institute of Robotics and Intelligent
Systems, Department of Mechanical and Process Engineering, ETH Zurich, Zurich,
Switzerland*

|| These authors contributed equally to this work.

E-mail: laeublin@ethz.ch

Abstract

Acoustically excited microstructures have demonstrated significant potential for small scale biomedical applications by overcoming major microfluidic limitations. Recently, the application of oscillating microbubbles has demonstrated their superiority over acoustically excited solid structures due to their enhanced acoustic streaming

at low input power. However, their limited temporal stability hinders their direct applicability for industrial or clinical purposes. Here, we introduce the embedded microbubble, a novel acoustofluidic design based on the combination of solid structures (polydimethylsiloxane) and microbubbles (air-filled cavity) to combine benefits of both approaches while minimizing their drawbacks. We investigate the influence of various design parameters and geometrical features through numerical simulations and experimentally evaluate their manipulation capabilities. Finally, we demonstrate the capabilities of our design for microfluidic applications by investigating its mixing performance as well as through the controlled rotational manipulation of individual HeLa cells.

Introduction

Precise manipulation capabilities at small scales are of increasing importance for a wide variety of research fields such as biomedicine or biology, *e.g.*, for the investigation of morphogenesis through single-cell analysis or detailed 3D reconstruction of complex model organisms.^{1,2} Therefore, it is not surprising that a large number of techniques have been introduced to facilitate the controlled rotation of small particles based on mechanical, magnetic, electrical, hydrodynamic, and optical forces.³ Unfortunately, many of these techniques rely on specific properties of the specimen, which significantly reduces their applicability for biological samples. The controlled particle manipulation using acoustic forces, acoustophoresis, has been widely applied due to its advantages of being label-free, contactless, and flexible in design while exposing biocompatible behaviour.⁴

Recent publications have illustrated a large variety of microstructures suitable for the controlled manipulation of single cells and particles through acoustic forces. Solid features such as polydimethylsiloxane (PDMS) or silicon sharp-edges are acoustically excited *via* an external piezoelectric transducer, leading to the formation of acoustic streaming patterns in the nearby liquid.⁵⁻⁸ Unfortunately, the majority of these acoustofluidic setups require a

high input power to generate acoustic fields that are strong enough to manipulate the specimens, which might damage biological samples.⁹ Additionally, depending on their design and arrangement, hydrophilic surface coatings are required to prevent the unintended formation of air bubbles which otherwise significantly alter the anticipated streaming patterns. Furthermore, most solid-feature-based designs are limited to the generation of in-plane vortices and are, therefore, unable to provide additional visual insights through the re-orientation of the specimen.

To overcome these challenges, microstreaming induced by an oscillating microbubble can be utilized. The streaming patterns of the microbubble can be switched from in-plane to out-of-plane streaming *via* altering the excitation frequency, allowing for controlled three-dimensional rotations of cells and organisms,^{10–13} as well as microfluidic applications including pumping or mixing.^{14–16} Due to its high compressibility and the corresponding strong oscillations, the microvortices produced by acoustically-activated microbubbles are significantly enhanced compared to the ones caused through the vibration of solid structures.^{17–19} However, the major drawback of microbubbles is their limited temporal stability. If acoustically excited, rectified diffusion leads to the bubble’s growth, which alters its resonance frequency and by that the strength and shape of the vortices.²⁰ This process can be decelerated using commercially available encapsulated bubbles; however, the instability of the thin polymer membrane of encapsulated bubbles complicates their application for long-term investigations.²¹ Lastly, as microbubbles are prone to be trapped in cavities due to hydrophilic/hydrophobic interactions, their dimensions show slight variations between multiple experiments, making it difficult to predict their precise response to acoustic excitation and preventing their use for clinical applications.

In this work, we introduce the embedded microbubble, a novel PDMS-based microstructure combining the low power advantage of bubble-based acoustic streaming with the temporal stability of acoustically-excited solid features. We perform in-depth numerical investigations and quantify the influence of geometrical parameters, such as the PDMS wall

thickness or the microbubble’s length, on the acoustic streaming inside the fluid channel and utilise these findings to optimise our device design. The manipulation capabilities of our acoustofluidic lab-on-chip are analysed through experimental characterisations and the revealed insights are discussed in further detail with respect to the numerical results. Finally, we highlight our device through the controlled and reliable out-of-plane rotation of single HeLa cells; a task beneficial to improve our understanding of biological processes on the cellular and sub-cellular level, and demonstrate the relevance of our approach for additional microfluidic applications through its use for mixing; a key step required for a wide variety of biomedical as well as chemical research.

Materials and Methods

Governing Equations

The force responsible for moving small (relative to the acoustic wavelength) particles in an acoustic field is called acoustic radiation force (ARF). For an inviscid fluid, it is given by the negative gradient of the Gor’kov potential²²

$$\mathbf{F}_{rad} = -\nabla U, \quad (1)$$

which can be expressed as:

$$U = \frac{4}{3}\pi r^3 \left(\frac{1}{2}\langle p^2 \rangle \frac{f_0}{c^2 \rho} - \frac{3}{4}\rho f_1 \langle v^2 \rangle \right), \quad (2)$$

with the particle radius r , the incident acoustic pressure field p , the acoustic velocity field v , the fluid speed of sound c , the density of the fluid ρ , the monopole f_0 and the dipole f_1 scattering coefficients. $\langle \cdot \rangle$ denotes time averaging

$$\langle x \rangle = \frac{1}{\tau} \int_{t_1}^{t_1+\tau} x dt, \quad (3)$$

where $\tau = \frac{2\pi}{\omega}$ is the period of oscillation, with angular frequency ω . The Gor'kov potential is derived under the assumption that boundaries are far away from the region of interest, which is not the case here. However, experimental studies revealed, that the theory should be valid up to close proximity of the embedded microbubble.²³

In acoustofluidics, the acoustic energy density is often used as a benchmark for the device's performance and, therefore, used in our numerical analysis. The average acoustic energy density (\overline{E}_{ac}) is given as²⁴

$$\overline{E}_{ac} = \frac{1}{V} \int_V \left(\frac{1}{2} \rho \langle v^2 \rangle + \frac{1}{2} \kappa \langle p^2 \rangle \right) dV, \quad (4)$$

with compressibility κ and volume V .

Another force that needs to be considered in our acoustofluidic chip is acoustic streaming, which affects a particle through a drag force:

$$\mathbf{F}_s = 6\pi\eta r (\mathbf{v}_{str} - \mathbf{v}_{prt}), \quad (5)$$

with the fluid dynamic viscosity η , particle radius r , streaming velocity \mathbf{v}_{str} and particle velocity \mathbf{v}_{prt} . The magnitude of the streaming velocity can be estimated as²⁵

$$|\mathbf{v}_{str}| = \psi \frac{v_a^2}{c}, \quad (6)$$

with the first order acoustic velocity v_a , the fluid speed of sound c , and the geometry dependant factor $\psi = \frac{3}{8}$ for a standing wave parallel to a planar wall.

Numerical Model

We built a 2D numerical model of the chip and evaluated it in COMSOL Multiphysics (version 5.4). We specifically studied the frequency response of the device. At resonance frequencies, we looked at the wall displacement as well as the Gor'kov potential and streaming

velocity. First, a mesh study was conducted, to determine the converged mesh parameters (see Figure S-1). After the initial frequency domain study of the Thermoviscous Acoustics and Solid Mechanics interface, a stationary study of the Creeping Flow interface at the resonance frequency was carried out by taking the solutions from the first study into account. With this study, we were able to investigate the streaming velocity. Please refer to the Supporting Information SI-1 for a more detailed description of the numerical model.

Device Fabrication

The polydimethylsiloxane (PDMS) device was fabricated using photolithography techniques (see Figure S-2) as well as a Bosch process with an inductively-coupled plasma deep reactive ion etching (ICP-DRIE) tool (PlasmaPro 100 Estrelas, *Oxford Instruments*). The etching mask consisted of a 7 μm thick AZ nLOF 2070 layer. The effect of prominent reactive ion etching (RIE) lag was reduced through iterative parameter optimisations following an approach introduced by Lai et al.²⁶ (see Supporting Information SI-2 and Figure S-3). The etch depth was $47.8 \pm 0.7 \mu\text{m}$. The processed silicon wafer was coated with silane (1H, 1H, 2H, 2H-Perfluorooctyltriethoxysilane, *abcr GmbH*) to ensure successful PDMS casting and prevent damage to the fragile polymer features. Subsequently, the designed structures were transferred into PDMS through moulding and chemically bonded to a microscope glass slide (AA00000102E01, *VWR International*) via oxygen plasma treatment. Finally, the transducer (KPEG-126, *Kingstate*) was fixed onto the glass slide using epoxy glue (UHU plus schnellfest, *UHU*).

Experimental Evaluation

Preliminary experiments to find the best excitation frequencies *via* attraction forces were performed with $10.29 \pm 1.01 \mu\text{m}$ fluorescence polystyrene particles (FSEG008, *Bangs Laboratories*). When strong resonances were found, yeast cells, *i.e.*, *Saccharomyces cerevisiae*, bought from a local supermarket, were submerged in de-ionised water and injected into

the microfluidic channel to be used as tracer particles for the acoustic streaming. Given the limited visual accessibility of the out-of-plane vortices, experimental evaluation relied on secondary in-plane streaming visualized by the yeast cell circulation near the embedded microbubbles.

The piezoelectric transducer has been excited *via* an arbitrary function generator (AFG3011C, *Tektronix*). The motion of the yeast cells has been captured at 12 – 17 frames/s using an inverted microscope (IX81, *Olympus*). To account for the varying size of yeast cells, multiple frames of the recordings were averaged. All data required for individual qualitative evaluations of design or process parameters has been collected in single experimental sessions to ensure comparability and to prevent inter-device discrepancies such as in the distance between the transducer and the PDMS device.

Our device’s mixing capabilities have been evaluated using normalised grey-scale analysis, with a standard deviation threshold of 10 % denoting sufficient mixing.²⁷ Mixing has been performed using a constant excitation frequency of 69 kHz. Steady volume flows of $0.3 \mu\text{l min}^{-1}$ and $0.66 \mu\text{l min}^{-1}$ for de-ionised water and black ink (4001, *Pelikan*) were achieved by syringe pumps (neMESYS, *Cetoni*).

Biological Model

HeLa S3 cells were cultured in RPMI 1640 (R5886, *Sigma Aldrich*) with 1x GlutaMAX (35050061, *Invitrogen*), supplemented with 10 % (v/v) Foetal Calf Serum (CVF5VF0001, *Eurobio Scientific*), $100 \mu\text{g ml}^{-1}$ penicillin/streptomycin (30-002-CI, *Corning*) and MEM non-essential amino acids solution (100x) (11140050, *Gibco*). The cells were grown at 37°C with 5 % CO_2 in a humidified incubator. Prior to their insertion into the chip, cells were detached *via* the addition of 0.05 % Trypsin-EDTA (1x) (25300096, *Gibco*).

Results & Discussion

Design Optimisation and Geometric Analysis

Accurate investigations and optimisations of design parameters are essential to ensure efficient and reliable manipulation capabilities in lab-on-chip applications. Figure 1 introduces our acoustofluidic device through the side (a) as well as the top (b) view. The main component consists of a polydimethylsiloxane (PDMS) feature that contains a microfluidic channel with dimension $D = 300 \mu\text{m}$ as well as the embedded microbubbles. The microbubbles have a constant width of $W = 100 \mu\text{m}$ but varying lengths L and are separated from the nearby liquid channel through thin PDMS walls with different thicknesses $T = 5 - 20 \mu\text{m}$. The PDMS device is excited *via* a piezoelectric transducer. By driving the transducer at specific frequencies, the thin PDMS wall between the microfluidic channel and the embedded microbubble can be brought to resonate in its eigenmodes, which subsequently allows for the attraction and rotation of small specimens in the nearby liquid.

To investigate the influence of the various geometrical design parameters onto the manipulation capabilities of the embedded microbubbles, features with different wall thicknesses $T = 5 - 20 \mu\text{m}$ and air chamber lengths $L = 500 - 1000 \mu\text{m}$ have been fabricated and the strength of the resulting acoustic effects has been evaluated qualitatively. For a device height H of $50 \mu\text{m}$, a smallest wall thickness of $T = 5 \mu\text{m}$ was chosen, which leads to an aspect ratio $H/T = 10$. Figure 1 c) shows two embedded microbubbles aligned along a microchannel with wall thicknesses T of $5 \mu\text{m}$ (B1) and $10 \mu\text{m}$ (B2). The initial analysis of our device revealed only minor changes in resonance frequencies between the different designs, a factor crucial for the subsequent in-depth experimental and numerical investigations.

Figure 1 d) shows polystyrene (PS) particles trapped near the acoustically excited microstructure. The wall thickness T of the embedded microbubble is $15 \mu\text{m}$ and the excitation parameters are 67.1 kHz and $10 V_{PP}$. The $10 \mu\text{m}$ PS particles remained in their stable positions while slowly rotating out-of-plane. The particles in the microchannel are only trapped

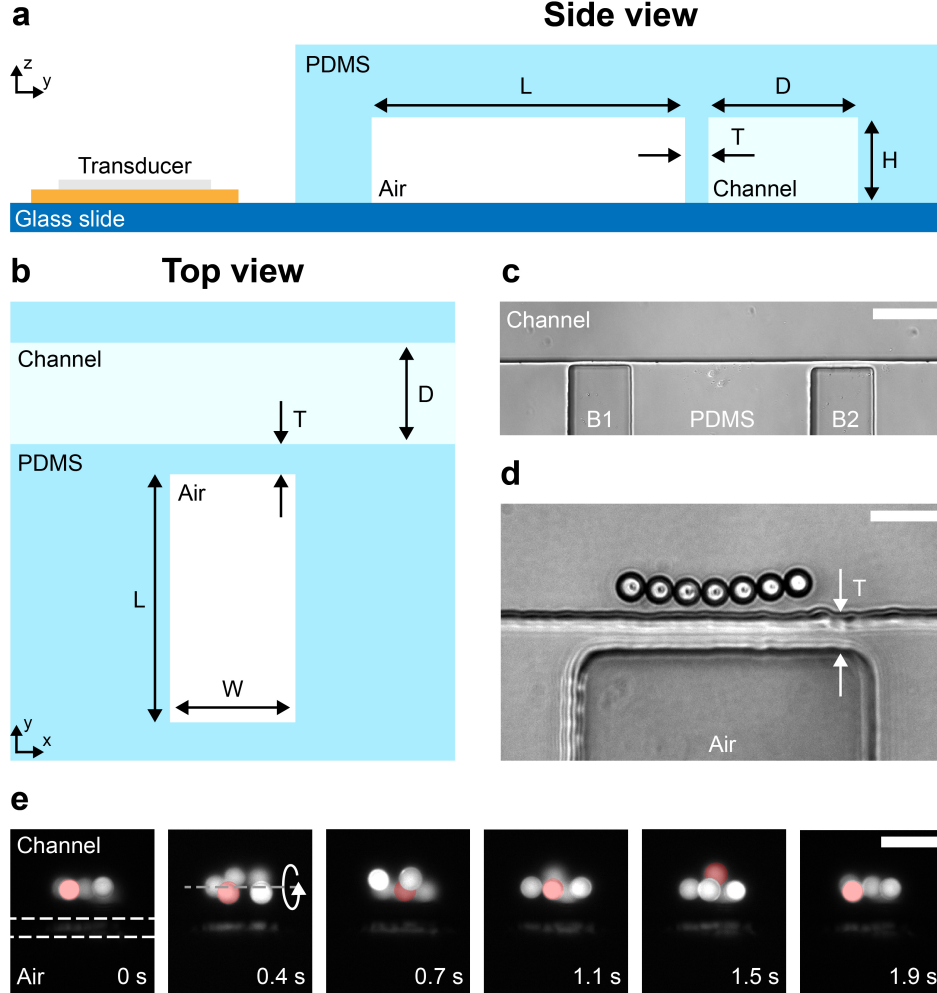


Figure 1: **Device layout and microscope pictures of particle attraction and rotation.** (a) Side view of a single embedded microbubble. The air trapped in a cavity is separated from the microchannel by a thin wall with thickness T . Four designs with different wall thicknesses $T = 5 - 20 \mu\text{m}$ have been fabricated. Additionally, the air chamber length L has been varied from $L = 500 - 1000 \mu\text{m}$. The height H of all features is approximately $50 \mu\text{m}$. (b) Top view of a single embedded microbubble with the numerically investigated wall thickness T , air chamber length L , and channel dimension D . The width W of the embedded microbubble was kept at $100 \mu\text{m}$. (c) Two embedded microbubbles B1 and B2 next to each other along the microchannel. B1 and B2 have a wall thickness T of $5 \mu\text{m}$ and $10 \mu\text{m}$, respectively. (d) Seven $10 \mu\text{m}$ PS particles trapped near an embedded bubble with $T = 15 \mu\text{m}$. The particles are slowly rotating out-of-plane. Particles were only trapped close to an embedded microbubble and not by the channel walls in general. (e) Fluorescent microparticles following an out-of-plane vortex in front of an embedded microbubble. A single particle is highlighted in red as it follows the streaming for two rotations. The white dashed lines indicate the location of the thin PDMS wall and the dashed grey line indicates the centre of rotation. Scale bars: $c = 100 \mu\text{m}$, $d = 25 \mu\text{m}$, $e = 25 \mu\text{m}$.

near the embedded microbubbles while not attracted by the regular walls of the microchannel, indicating that the effect is not induced through the general PDMS-liquid interface. Furthermore, Figure 1 e) presents an image sequence of out-of-plane rotating PS particles close to an embedded microbubble with a wall thickness T of $15\ \mu\text{m}$ (white dashed lines in the first image). The excitation frequency and voltage are $68\ \text{kHz}$ and $10\ V_{PP}$, respectively. The demonstrated motion of the microparticles is further presented in Supporting Information SV-1, which highlights our feature’s capability to generate stable out-of-plane vortices reliably; a crucial task for single-cell analysis as well as the investigation of small model organisms.

Following our preliminary experimental analysis, we performed numerical investigations of the various designs to optimise the device’s performance. Figure 2 a) shows the simulated wall displacements for varying wall thicknesses T . As our investigations focused on the region near the embedded microbubble, the streaming velocity (Eq. 6) and the acoustic energy density (Eq. 4) have been integrated and averaged over the hatched area of $50\times 50\ \mu\text{m}$. The simulation results suggest that the wall thickness and wall displacement are inversely proportional with thinner walls demonstrating higher displacement amplitudes than thicker walls for the same excitation voltage. The simulations have been performed at each structure’s corresponding mode with the largest displacement, which correlates nicely to the highest acoustic energy density. The modes have been chosen based on preliminary experimental observations that suggested strong acoustic interactions for excitations around a frequency of $69\ \text{kHz}$. Surprisingly, the numerical investigations revealed only minor variations of the frequency ($69.05\pm 0.02\ \text{kHz}$) with the strongest displacement for the various wall thicknesses. The minor variations of the frequency indicate that the amplitude of the wall’s displacement is not solely dependant on the wall thickness but further significantly influenced by the geometry of the air, water, and PDMS components. This assumption was further verified by an extended frequency sweep for all wall thicknesses. Supporting Figures S-4, S-5, and S-6

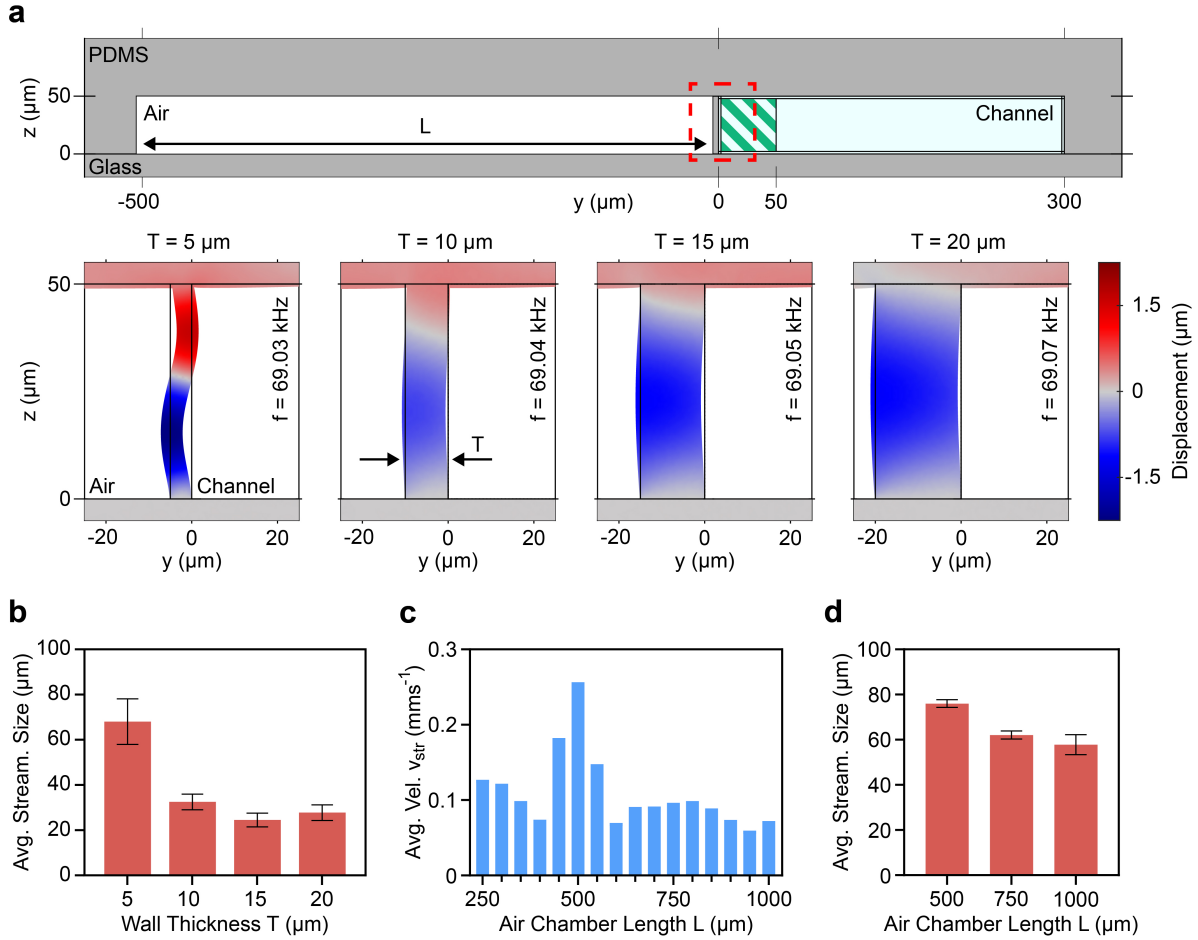


Figure 2: Design optimization with numerical and experimental investigations. (a) Numerical model of the device’s yz -plane zoomed in to highlight the embedded microbubble and water channel. The region of interest, containing the thin PDMS wall, is highlighted with a red square. The green hatched area near the PDMS wall inside the fluid channel denotes the area used for the numerical evaluation of the average acoustic energy density E_{ac} as well as the average streaming velocity v_{str} . The wall displacement for varying wall thicknesses $T = 5 - 20 \mu\text{m}$ have been derived through numerical simulations. While thinner walls lead to stronger displacements, similar resonance frequencies of the thicker walls have been observed, indicating that the resonance of the bubble dominates. (b) Experimentally determined in-plane streaming sizes (in y -direction) for different wall thicknesses T with a constant air chamber length $L = 500 \mu\text{m}$. The largest streaming pattern has been observed for a wall thickness of $T = 5 \mu\text{m}$. (c) Numerical results for the average streaming velocity v_{str} at the resonance frequency for air chamber lengths $L = 250 - 1000 \mu\text{m}$ with a constant wall thickness $T = 5 \mu\text{m}$. The maximum average streaming velocity in the area close to the vibrating wall is achieved for an air chamber length of $L = 500 \mu\text{m}$. (d) Experimental results of the in-plane streaming size for different air chamber lengths L and a constant wall thickness $T = 5 \mu\text{m}$. The experimental results nicely fit the findings of the numerical investigations, indicating that $L = 500 \mu\text{m}$ leads to the largest streaming vortices.

display the typical S-shaped resonances of the different geometries. It is important to note that, despite being in resonance, the amplitudes of their vibrations decrease for increasing excitation frequency. Since the decrease in displacement is mainly independent of the wall's geometry, the investigated vibrations are likely dominated by the resonances of the embedded microbubbles.

Subsequently, we performed experimental characterisations of the strong dependence between wall thickness and wall displacement highlighted by the numerical simulations. As a measure for comparison between the different geometries, yeast cells have been introduced into the microchannel as tracer particles. The sizes of the resulting in-plane streaming vortices were taken as a measure for comparison. A channel dimension $D = 300 \mu\text{m}$ has been chosen to avoid interference between the local acoustic streaming at the embedded microbubble and the opposing wall. As can be seen in Figure 2 b), significantly larger streaming patterns have been achieved for embedded microbubbles with $5 \mu\text{m}$ walls than for designs with thicker features. It is important to highlight that all embedded microbubbles were located on the same device and arranged next to each other along the microchannel, as shown in Figure 1 c), to prevent possible inaccuracies in the results due to variations in the setup. Additionally, all features have been evaluated around an excitation frequency of 66 kHz and voltage of $20 V_{PP}$ with only minor distinctions between resonance peaks being possible through visual observations. Excitation of the device at significantly higher or lower frequencies did lead to none or only minor acoustic streaming, indicating that the wall has a limited activity at other frequencies as expected by our numerical analysis (see Supporting Figure S-4, S-5, and S-6). While no clear differences in the streaming patterns have been observed for the wall thicknesses of $T = 10 - 20 \mu\text{m}$, higher input power might be required to allow for a clear distinction of the influence of this geometrical parameter.

Following the quantification of the wall thickness' effect on the acoustic capabilities of our device, we proceeded with the investigation of the influence of the air chamber length L .

In numerical simulations, the air chamber length L has been increased from 250 to 1000 μm with steps of 50 μm . Figure 2 c) indicates that the strongest average streaming velocity can be expected for $L = 500 \mu\text{m}$. At this air chamber length, the surrounding PDMS seems to compress the embedded air in a way that supports the vibrational mode of the resonating thin wall. However, further investigations are needed to evaluate the influence of the air chamber length properly. Additionally, we cannot fully exclude other factors such as large scale deformations of the PDMS device due to overall changes in the stability of the features. Subsequently, the influence of the air chamber length L has been quantified experimentally (Figure 2 d)). All microstructures have been excited using the same parameters, *i.e.*, frequency and voltage, and the sizes of the generated in-plane vortices have been measured. While the experimentally obtained results expose a similar trend as predicted by the numerical simulations, the superiority regarding streaming size of $L = 500 \mu\text{m}$ is less pronounced in experiments, therefore further investigations might be necessary to allow for the appropriate interpretation of these results. A non-negligible reason for the variation observed between the numerically determined results and the experimental quantifications might also be based on differences in the evaluated quantity. While the numerical simulations allow for a direct investigation of the streaming velocity of the produced out-of-plane streaming near the embedded microbubble, due to limited accessibility to this streaming during experimental evaluations, the latter has to rely on the generated in-plane vortices. Therefore, the comparison of the results obtained through the different techniques, *i.e.*, numerical and experimental evaluations, might be restricted by the complex and possibly non-linear relationship between the out-of-plane and the in-plane streaming vortices.

Investigation of Acoustofluidic Capabilities

Based on the results presented in the device optimisation, we opted for a design with wall thickness $T = 5 \mu\text{m}$ and air chamber length $L = 500 \mu\text{m}$ and performed more specific numerical analyses to gain further insights regarding the underlying mechanisms and the acoustic

phenomena. Figure 3 a) shows the average wall displacement and the average acoustic energy density for frequencies from 40 to 90 kHz with 100 Hz steps. The maximal energy density correlates with the highest displacement of the wall and reveals two strong resonances (41.89 kHz and 69.03 kHz). Experimental investigations showed that frequencies around 69 kHz lead to much stronger particle attraction and streaming velocities than frequencies around 40 kHz. The deviation from observed and simulated resonance frequency can be attributed to idealised material parameters and the limited significance of the displacement boundary condition, *e.g.*, through lower amplitudes of the piezoelectric element at this frequency range. However, the aim of the numerical investigations is not to attain exact amplitudes but to show trends and get insight into the physical phenomena of the device.

At the resonance frequency of 69.03 kHz, a strong fluid vortex is generated close to the thin wall that drives the fluid in a counter-clockwise fashion, which is ranging up to 50 μm into the channel (see Figure 3 b)) and could be utilised for controlled particle rotation. However, the particle needs to be positioned close to the thin wall to be influenced by the streaming vortex, which can be achieved by the acoustic radiation force. For particle attraction towards the thin wall, the Gor'kov potential minimum needs to be close to the embedded microbubble (see Equation 1). As can be seen in Figure 3 c), at the resonance frequency of 69.03 kHz a Gor'kov potential minimum is generated at half of the height of the thin wall; thus, particles are attracted to the displacement node of the thin PDMS wall. It is important to highlight, that the generated node is not based on a standing wave formation inside the channel and, thereby, does not rely on the geometrical dimensions of the PDMS as a whole.²⁸

Figure 3 d) shows the experimentally evaluated relation between the out-of-plane rotational speed of a specimen and the applied excitation voltage. The embedded microbubble has been excited at a constant frequency of 69.2 kHz, which is in great accordance with the numerically detected maximal wall displacements around that frequency. The rotational

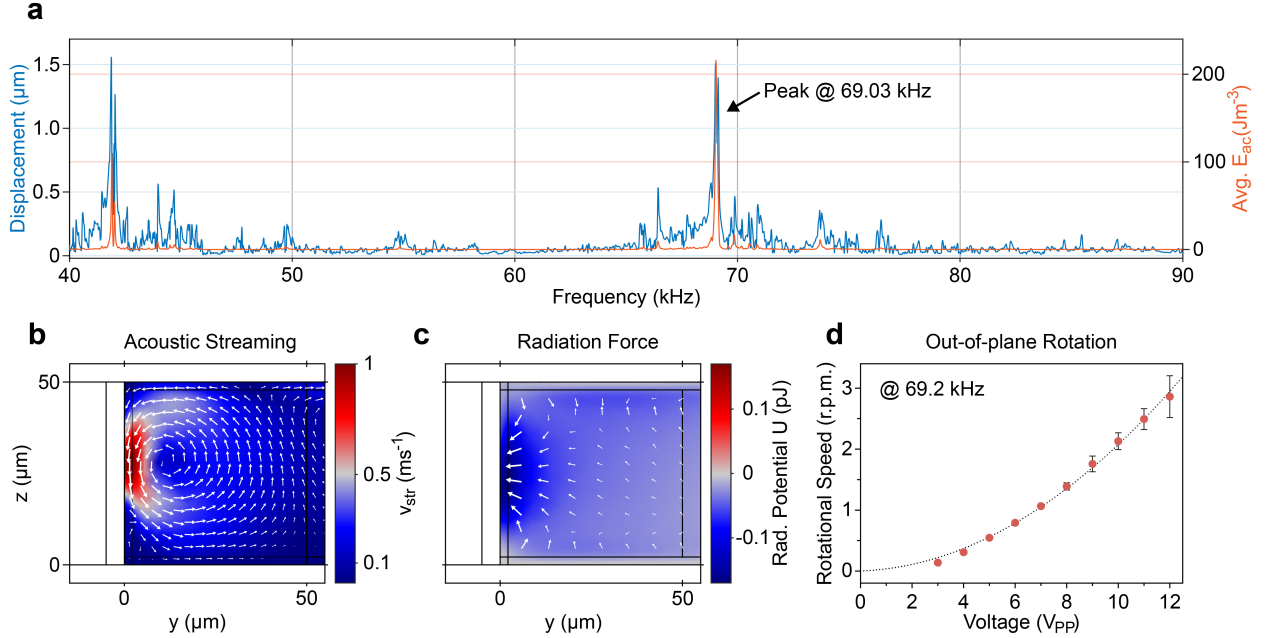


Figure 3: **Detailed investigation of a device with wall thickness $T = 5 \mu\text{m}$ and embedded microbubble length $L = 500 \mu\text{m}$.** (a) Frequency sweep from 40 to 90 kHz with steps of 0.1 kHz. The displacement of the thin PDMS wall and the average acoustic energy density E_{ac} show prominent resonances at 41.89 kHz and 69.03 kHz. (b) Streaming velocity field near the thin PDMS wall. The velocity of the acoustic streaming is strongest close to the wall and drives the fluid in a counter-clockwise fashion. (c) Gor'kov potential as well as the acoustic radiation force (white arrows). The minimum of the Gor'kov potential can be found at half the height of the thin wall. Therefore, the acoustic radiation force is pointing towards this position, which, in experiments, leads to a particle attraction from the channel towards the embedded microbubble. Both (b) and (c) were simulated with an excitation frequency of 69.03 kHz, which is corresponding to the strongest resonance. (d) The experimentally determined relationship between the excitation voltage and the out-of-plane rotational speed of a specimen (rotation around x-axis). While the excitation frequency is kept constant at 69.2 kHz, an increase of the input power leads to stronger streaming velocities (Eq. 6) and subsequently to faster rotations of the specimen. The dashed line denotes a fitted quadratic curve with a coefficient of determination $R^2 = 0.98$.

speed follows the input voltage in a quadratic dependency ($R^2 = 0.98$), demonstrating our approach's high controllability of the specimens orientation which is crucial for biomedical applications such as single-cell analysis. It is important to note that the increasing error at high voltages might be induced through uncertainties based on frame rate limitations of the experimental setup. However, additional sources, including possible cell membrane instabilities or the motion of intracellular features during fast rotational manipulations, can

not be excluded.

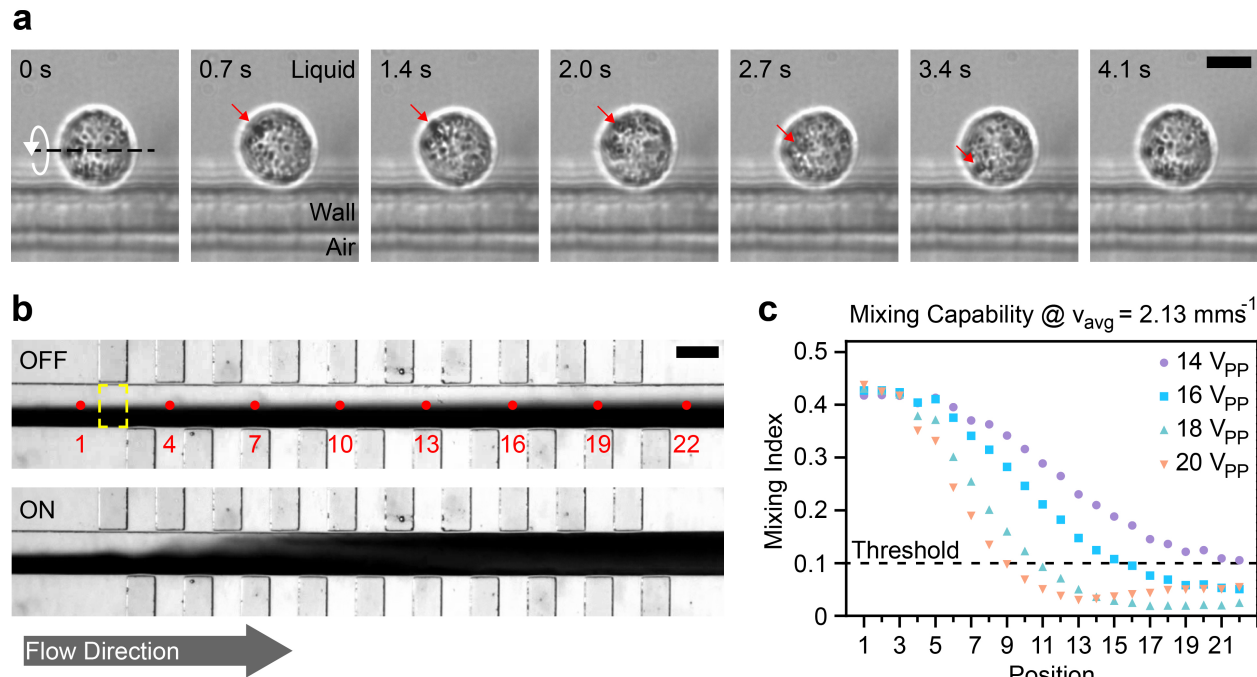


Figure 4: **Microfluidic applications for embedded microbubbles.** (a) The controlled out-of-plane rotation of a single HeLa cell. The microstructure is excited at a constant frequency and voltage of 69.2 kHz and 5 V_{PP} , respectively. The white arrow denotes the direction of the specimen’s rotation while the red arrow highlights a spot on the specimen’s surface. (b) Microfluidic mixing of two liquids in a 150 μm wide microchannel based on acoustically activated embedded microbubbles. The top image shows the laminar flow of the liquid where mixing is limited to diffusion. The red dots show the positions along the microchannel used for the evaluation of the efficiency. The yellow rectangle indicates the area used for the calculation of the mixing index at position 2. The bottom image demonstrates the mixing procedure for an excitation voltage of 20 V_{PP} and a flow velocity of $v_{avg} = 2.13 \text{ mm s}^{-1}$. (c) Experimental evaluation of the mixing index for different input voltages. The mixing index corresponds to the standard deviation of the normalised grey-scale image at the corresponding positions of the microchannel. The horizontal line at 10% denotes sufficient mixing. Scale bars: (a) = 10 μm , (b) = 150 μm .

Single-Cell Manipulation and Microfluidic Mixing

We expand the investigation of our device by demonstrating its application for two diverse applications, *i.e.*, single-cell manipulation as well as microfluidic mixing. HeLa cells are a prominent model organism for biomedical as well as genetic research^{29,30} and their controlled

manipulation exposes great potential to allow for further insights on a single cell level.³

The image sequence in Figure 4 a) presents the slow and stable out-of-plane rotation of a single HeLa cell near an embedded microbubble with a wall thickness $T = 5 \mu\text{m}$, while the piezoelectric transducer is excited with a constant frequency of 69.2 kHz and voltage of $5 V_{PP}$. The HeLa cell's motion is further presented in Supporting Information SV-2. Please note that, in contrast to many solid microstructures used for acoustic manipulation,³¹ the demonstrated rotational motion has been achieved at a low excitation voltage of $6 V_{PP}$, thereby preventing possible damage to the sample due to high power pressure fields. The successful manipulation of the HeLa cell is based on the combination of the acoustic radiation force and acoustic streaming. As demonstrated through the numerical simulations, the Gor'kov potential (see Figure 3 c)) leads to a force which pushes biological specimens towards the embedded microbubble. Once trapped, the single cell is rotated *via* the viscosity-related acoustic streaming, which allows for the visual investigation of the specimens intracellular components as well as individual features of the cell membrane. Please note that the wall thickness appears larger in the image sequence due to the plane of focus being set on the specimen.

Due to the flow limitations at the low Reynolds regime, reliable mixing is essential for a variety of lab-on-chip applications in chemical as well as biomedical analysis.³²⁻³⁴ Our acoustic-based mixer consists of a series of alternating embedded microbubbles with wall thickness $T = 5 \mu\text{m}$ arranged along a single microchannel. The channel dimension D has been set to $150 \mu\text{m}$ based on numerical investigations to ensure strong and local streaming near the microstructures. Two liquids, *i.e.*, de-ionised water and blue ink, are introduced through separated channels while their volume flow is controlled *via* a high-precision microfluidic pumping system to achieve an average flow velocity v_{avg} . The inlet channels meet at an angle of 90° to minimise diffusion-based mixing while avoiding possible acoustic streaming near sharp-edge features.^{5,35,36}

Figure 4 b) shows the PDMS device with the two laminar flows prior to acoustic excitation, *i.e.*, the piezoelectric transducer is off, as well as during mixing of two fluids using an input voltage of $20 V_{PP}$ (see Supporting Information SV-3). The average flow velocity inside the microchannel is $v_{avg} = 2.13 \text{ mm s}^{-1}$, which, despite requiring significantly lower input power and not relying on surface treatments, is comparable to results presented for solid-structure-based acoustic mixers.^{27,37,38} Additionally, as our design allows to prevent geometrical constrictions, unintended trapping of microbubbles inside the mixing channel can be avoided. While bubble-based acoustic mixers allow for increased handling of fluid volumes, our approach circumvents their limitations in temporal stability and re-usability.^{14,39,40} The graph in Figure 4 c) demonstrates the experimentally determined relationship between the applied input power and the acoustic manipulation capabilities of our device. To allow for the evaluation of device performance, we calculated the mixing indices at different positions of the microchannel, starting with position 1 in front of the mixer (see red labels in Figure 4 b)). For each position, a mixing index has been derived as the standard deviation of the normalised grey-scale image (area highlighted with yellow lines). A threshold of 10 % has been defined as sufficient mixing based on previous literature.²⁷ The graph demonstrates that, for our design with 20 alternating embedded microbubbles and for average flow velocities $v_{avg} = 2.13 \text{ mm s}^{-1}$, successful mixing can be achieved for excitation voltages as low as $16 V_{PP}$ (blue squares) while, for $20 V_{PP}$ (orange triangle), the threshold is already reached after 8 features.

To allow for direct comparison between various designs and techniques applied in microfluidic mixing, the average mixing time can be derived as

$$\tau_S = L_{mix}/v_{avg} \approx 376 \text{ ms} \quad (7)$$

where $L_{mix} = 800 \mu\text{m}$ is the mixing distance required to achieve sufficient mixing for an excitation voltage of $20 V_{PP}$. However, it is important to note that the device's efficiency

might be further improved through design optimisations, such as by arranging the embedded bubbles in an opposite instead of an alternating manner. Additionally, as active streaming has only been observed directly in front of the embedded microbubbles, the distance between the features could be reduced without leading to unintended and possibly unfavorable interactions between the generated vortices. Furthermore, through the simple application of an external amplifier, the strength of the acoustic streaming could be further increased, which would allow to reduce the derived mixing distance.

Conclusion & Outlook

In this work, we introduced a novel acoustofluidic device combining the advantages of solid and bubble-based features and demonstrated its use for particle and single-cell manipulation as well as microfluidic applications. We numerically investigated different geometrical design parameters and derived their complex relationship to the acoustically generated streaming pattern. Then, following noticeable fabrication improvements, we successfully confirmed our observations through experimental characterisations. Optimum device performance with regards to its out-of-plane rotation capabilities has been numerically determined for a microbubble length of 500 μm , wall width of 5 μm , and fluid channel width of 150 μm .

We explored the applicability of our device for biomedical research through the controlled out-of-plane rotation of single HeLa cells and quantified the near quadratic dependency between the applied voltage and the specimen's rotational speed, which allows for the high controllability necessary to achieve slow yet stable motions crucial for future biological investigations, *e.g.*, through fluorescence imaging. Finally, we illustrated our lab-on-chip sub-second mixing performance and discussed potential design improvements for increased efficiency. Nevertheless, it is worth highlighting that the current achievements are comparable to previous publications while relying on significantly lower input power and maintaining the microbubble's temporal stability.

Future work may include mixing-based gradient generation important for various chemical applications and the extension of our approach for manipulating multi-cellular organisms, such as *Caenorhabditis elegans*.

Acknowledgement

The authors would like to express their gratitude to Alen Pavlic and Thierry Baasch for their valuable contributions to the numerical simulation. This work is supported by the ETH Zurich and, in part, by an interdisciplinary grant from the Swiss National Science Foundation (Grant Number CR22I2_166110) to B.J.N., a grant from the Swiss National Science Foundation (Grant Number 310030_184801) to U.K., and the ETH Zurich Career Seed Grant-14 17 – 2 to D.A..

Supporting Information Available

Supplementary Material Available: Details on the the numerical model and its mesh study, the fabrication procedure and optimisation, and videos on the manipulation capabilities.

References

- (1) Luo, T.; Fan, L.; Zhu, R.; Sun, D. Microfluidic Single-Cell Manipulation and Analysis: Methods and Applications. *Micromachines* **2019**, *10*, 104.
- (2) Chen, C.; Gu, Y.; Philippe, J.; Zhang, P.; Bachman, H.; Zhang, J.; Mai, J.; Rufo, J.; Rawls, J. F.; Davis, E. E.; Katsanis, N.; Huang, T. J. Acoustofluidic rotational tweezing enables high-speed contactless morphological phenotyping of zebrafish larvae. *Nature Communications* **2021**, *12*.

- (3) Tang, T.; Hosokawa, Y.; Hayakawa, T.; Tanaka, Y.; Li, W.; Li, M.; Yalikun, Y. Rotation of Biological Cells: Fundamentals and Applications. *Engineering* **2021**,
- (4) Laurell, T., Lenshof, A., Eds. *Microscale Acoustofluidics*; The Royal Society of Chemistry, 2015; pp P001–574.
- (5) Doinikov, A.; Gerlt, M.; Pavlic, A.; Dual, J. Acoustic streaming produced by sharp-edge structures in microfluidic devices. *Microfluid Nanofluid* **2020**, *24*, 32.
- (6) Feng, L.; Song, B.; Chen, Y.; Liang, S.; Dai, Y.; Zhou, Q.; Chen, D.; Bai, X.; Feng, Y.; Jiang, Y.; Zhang, D.; Arai, F. On-chip rotational manipulation of microbeads and oocytes using acoustic microstreaming generated by oscillating asymmetrical microstructures. *Biomicrofluidics* **2019**, *13*, 064103.
- (7) Leibacher, I.; Hahn, P.; Dual, J. Acoustophoretic cell and particle trapping on microfluidic sharp edges. *Microfluid Nanofluid* **2015**, *19*, 923–933.
- (8) Huang, P.-H.; Nama, N.; Mao, Z.; Li, P.; Rufo, J.; Chen, Y.; Xie, Y.; Wei, C.-H.; Wang, L.; Huang, T. J. A reliable and programmable acoustofluidic pump powered by oscillating sharp-edge structures. *Lab Chip* **2014**, *14*, 4319–4323.
- (9) Wang, Z.; Huang, P.-H.; Chen, C.; Bachman, H.; Zhao, S.; Yang, S.; Huang, T. J. Cell lysis via acoustically oscillating sharp edges. *Lab on a Chip* **2019**, *19*, 4021–4032.
- (10) Marmottant, P.; Hilgenfeldt, S. Controlled vesicle deformation and lysis by single oscillating bubbles. *Nature* **2003**, *423*, 153–156.
- (11) Ahmed, D.; Ozcelik, A.; Bojanala, N.; Nama, N.; Upadhyay, A.; Chen, Y.; Hanna-Rose, W.; Huang, T. J. Rotational manipulation of single cells and organisms using acoustic waves. *Nature Communications* **2016**, *7*.
- (12) Läubli, N. F.; Shamsudhin, N.; Vogler, H.; Munglani, G.; Grossniklaus, U.; Ahmed, D.;

- Nelson, B. J. 3D Manipulation and Imaging of Plant Cells using Acoustically Activated Microbubbles. *Small Methods* **2019**, *3*, 1800527.
- (13) Li, Y.; Liu, X.; Huang, Q.; Arai, T. Controlled rotation of micro-objects using acoustically driven microbubbles. *Applied Physics Letters* **2021**, *118*, 063701.
- (14) Tovar, A. R.; Lee, A. P. Lateral cavity acoustic transducer. *Lab Chip* **2009**, *9*, 41–43.
- (15) Okabe, Y.; Lee, A. P. LCAT DNA Shearing. *Journal of Laboratory Automation* **2014**, *19*, 163–170, PMID: 23850863.
- (16) Jiang, R.; Agrawal, S.; Aghaamoo, M.; Parajuli, R.; Agrawal, A.; Lee, A. P. Rapid isolation of circulating cancer associated fibroblasts by acoustic microstreaming for assessing metastatic propensity of breast cancer patients. *Lab Chip* **2021**, Advance Article.
- (17) Nyborg, W. L. Acoustic Streaming near a Boundary. *The Journal of the Acoustical Society of America* **1958**, *30*, 329–339.
- (18) Manasseh, R. *Handbook of Ultrasonics and Sonochemistry*; Springer Singapore, 2016; pp 33–68.
- (19) Lu, H.-F.; Tien, W.-H. Comparison of Acoustic Streaming Flow Patterns Induced by Solid, Liquid and Gas Obstructions. *Micromachines* **2020**, *11*, 891.
- (20) Volk, A.; Rossi, M.; Kähler, C. J.; Hilgenfeldt, S.; Marin, A. Growth control of sessile microbubbles in PDMS devices. *Lab Chip* **2015**, *15*, 4607–4613.
- (21) Liu, Y.; Calvisi, M. L.; Wang, Q. Shape oscillation and stability of an encapsulated microbubble translating in an acoustic wave. *The Journal of the Acoustical Society of America* **2018**, *144*, 2189–2200.
- (22) Gorkov, L. On the forces acting on a small particle in an acoustical field in an ideal fluid. *Phys.-Dokl.* **1962**, *6*, 773–775.

- (23) Miller, D. L. Particle gathering and microstreaming near ultrasonically activated gas-filled micropores. *The Journal of the Acoustical Society of America* **1988**, *84*, 1378–1387.
- (24) Pierce, A. D. *Acoustics : an introduction to Its physical principles and applications*, 3rd ed.; Springer International Publishing: Woodbury, 1991.
- (25) Bruus, H. Acoustofluidics 10: Scaling laws in acoustophoresis. *Lab Chip* **2012**, *12*, 1578–1586.
- (26) Lai, S. L.; Johnson, D.; Westerman, R. Aspect ratio dependent etching lag reduction in deep silicon etch processes. *Journal of Vacuum Science & Technology A: Vacuum, Surfaces, and Films* **2006**, *24*, 1283–1288.
- (27) Huang, P.-H.; Xie, Y.; Ahmed, D.; Rufo, J.; Nama, N.; Chen, Y.; Chan, C. Y.; Huang, T. J. An acoustofluidic micromixer based on oscillating sidewall sharp-edges. *Lab Chip* **2013**, *13*, 3847–3852.
- (28) Moiseyenko, R. P.; Bruus, H. Whole-System Ultrasound Resonances as the Basis for Acoustophoresis in All-Polymer Microfluidic Devices. *Physical Review Applied* **2019**, *11*.
- (29) Liu, Y. et al. Multi-omic measurements of heterogeneity in HeLa cells across laboratories. *Nature Biotechnology* **2019**, *37*, 314–322.
- (30) Luithle, N.; uit de Bos, J.; Hovius, R.; Maslennikova, D.; Lewis, R. T.; Ungricht, R.; Fierz, B.; Kutay, U. Torsin ATPases influence chromatin interaction of the Torsin regulator LAP1. *eLife* **2020**, *9*.
- (31) Ozcelik, A.; Nama, N.; Huang, P.-H.; Kaynak, M.; McReynolds, M. R.; Hanna-Rose, W.; Huang, T. J. Acoustofluidic Rotational Manipulation of Cells and Organisms Using Oscillating Solid Structures. *Small* **2016**, *12*, 5120–5125.

- (32) Lee, C.-Y.; Chang, C.-L.; Wang, Y.-N.; Fu, L.-M. Microfluidic Mixing: A Review. *International Journal of Molecular Sciences* **2011**, *12*, 3263–3287.
- (33) Bayareh, M.; Ashani, M. N.; Usefian, A. Active and passive micromixers: A comprehensive review. *Chemical Engineering and Processing - Process Intensification* **2020**, *147*, 107771.
- (34) Tomeh, M. A.; Zhao, X. Recent Advances in Microfluidics for the Preparation of Drug and Gene Delivery Systems. *Molecular Pharmaceutics* **2020**, *17*, 4421–4434.
- (35) Cheng, W.; Erbay, C.; Sadr, R.; Han, A. Dynamic Flow Characteristics and Design Principles of Laminar Flow Microbial Fuel Cells. *Micromachines* **2018**, *9*, 479.
- (36) Läubli, N.; Shamsudhin, N.; Ahmed, D.; Nelson, B. J. Controlled Three-dimensional Rotation of Single Cells Using Acoustic Waves. *Procedia CIRP* **2017**, *65*, 93–98.
- (37) Zhang, C.; Guo, X.; Brunet, P.; Costalonga, M.; Royon, L. Acoustic streaming near a sharp structure and its mixing performance characterization. *Microfluidics and Nanofluidics* **2019**, *23*.
- (38) Zhang, C.; Guo, X.; Royon, L.; Brunet, P. The effect of sharp-edge acoustic streaming on mixing in a microchannel. **2020**,
- (39) Ahmed, D.; Mao, X.; Juluri, B. K.; Huang, T. J. A fast microfluidic mixer based on acoustically driven sidewall-trapped microbubbles. *Microfluidics and Nanofluidics* **2009**, *7*, 727–731.
- (40) Ahmed, D.; Mao, X.; Shi, J.; Juluri, B. K.; Huang, T. J. A millisecond micromixer via single-bubble-based acoustic streaming. *Lab on a Chip* **2009**, *9*, 2738.

Graphical TOC Entry

